Investigation of high-temperature plastic deformation using instrumented microindentation tests. Part II: The deformation of Al-based particulate reinforced composites at 473 K to 833 K

V. BHAKHRI, R.J. KLASSEN*
Department of Mechanical and Materials Engineering, Faculty of Engineering, University of Western Ontario, London, Ontario N6A 5B9, Canada
E-mail: rklassen@eng.uwo.ca

Published online: 3 March 2006

Constant-load pyramidal indentation tests were performed from 473 K to 833 K on P/M fabricated 2024 aluminum reinforced with either SiO_2, SiC, or Al_2O_3 particles to investigate the influence of particulate reinforcement on the high-temperature plastic deformation process during indentation. The composites all displayed larger apparent threshold stress σ_{th} than the previously reported unreinforced P/M 2024 aluminum alloy. SEM investigation of the indentations indicated that the indentation process is accompanied by considerable cracking and interfacial debonding of the reinforcing particles, the extent of which increases with increasing temperature. The magnitude of σ_{th} was largest for the Al_2O_3 reinforced composite and this is attributed to the load-transfer that occurs when the indenter contacts the reinforcing particles and the superior high-temperature interfacial strength of this composite. The apparent activation energy ΔG_0 of the indentation strain rate increased from $0.25\mu b^3$ at 473 K to $0.60\mu b^3$ at 833 K. These values are within the expected range for weak particles and dislocation-dislocation interactions but are lower than the previously reported Δ_0 of the unreinforced P/M 2024 alloy. We conclude that the low indentation strain rate of the particulate reinforced composites is the result of the load transfer due to the presence of the reinforcements and its affect on increasing the σ_{th}. The low values of ΔG_0 are consistent with our observation that extensive particle cracking and interfacial debonding occur in the reinforced material during indentation.

1. Introduction

The high-temperature deformation mechanisms that operate in aluminum matrix particulate-reinforced composites have been studied extensively for many years [1–9]. The bulk of what is known about the stress- and temperature-dependence of the deformation rate of this material results from uniaxial stress experiments performed under conditions of either constant stress or constant strain rate. It is generally observed that there exists in these materials a large threshold stress σ_{th} below which the strain rate approaches zero. This σ_{th} has been attributed to the presence of the reinforcing particles although the mechanism by which the particles constrain the deformation is still not universally accepted. For example, Wilkinson and Artz [10], following a technique of Shewfelt and Brown [11], proposed that the threshold shear stress in dispersion hardened metal alloys is inversely related to the inter-particle spacing l. Other observations, which are based primarily upon room temperature tensile testing, suggest that the role of particulate reinforcements in dispersion hardened metals is complicated by various other factors including clustering, cracking, and interfacial debonding of the reinforcing particles [12–14].

*Author to whom all correspondence should be addressed.
0022-2461
DOI: 10.1007/s10853-006-7175-6

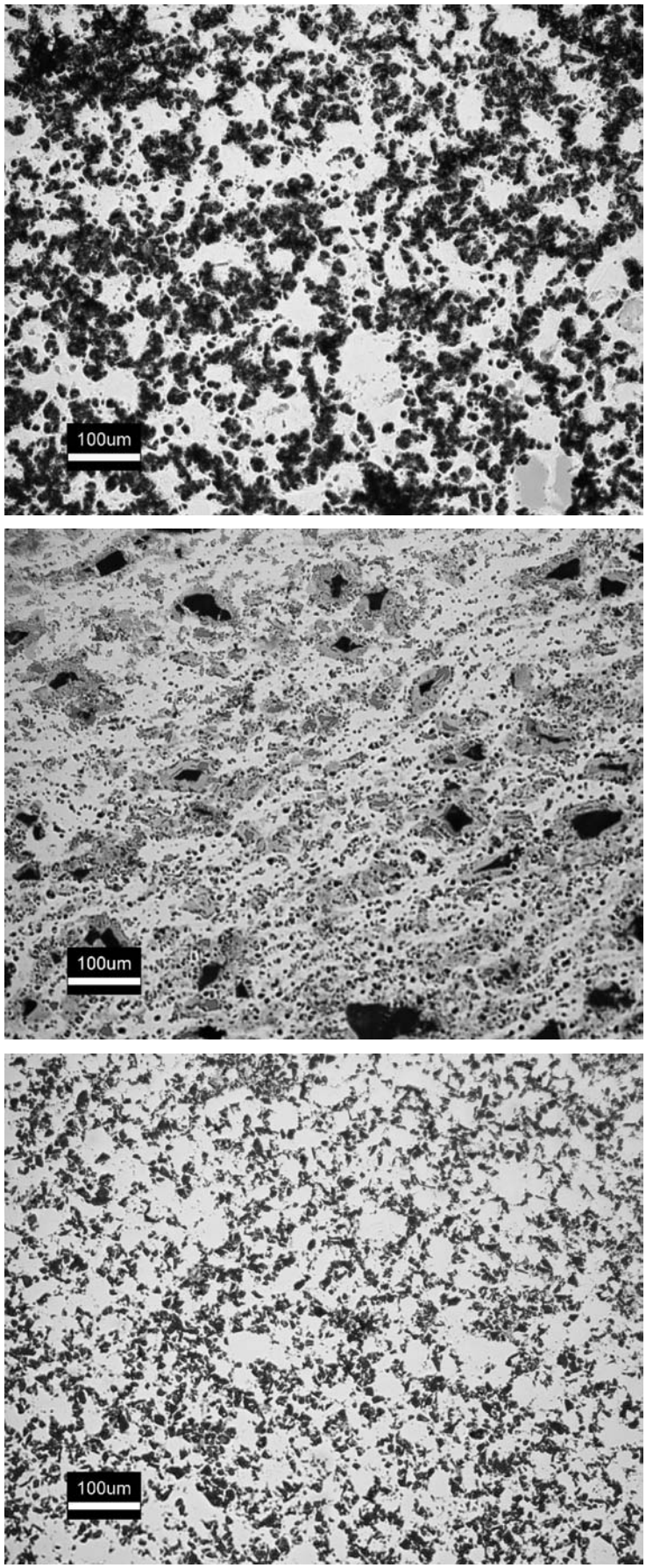

Figure 1 Optical Micrographs of the microstructure of the three particulate reinforced P/M 2024 aluminum alloy based composites used in this investigation: (a) SiC reinforced composite, (b) SiO_2 reinforced composite and (c) Al_2O_3 reinforced composite.

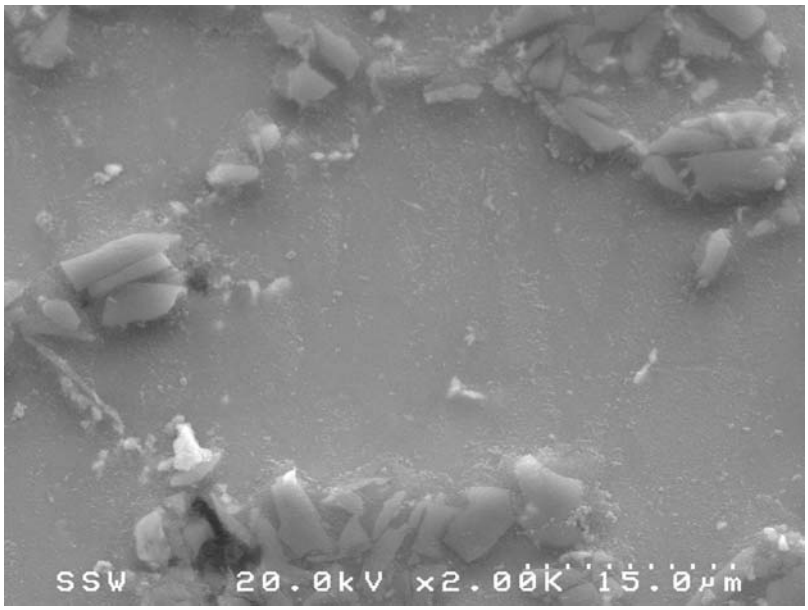

Figure 2 Scanning Electron Micrographs of the SiC reinforced 2024 P/M aluminum alloy composite. The SiC reinforcing particles are distributed around the periphery of the starting aluminum powder.

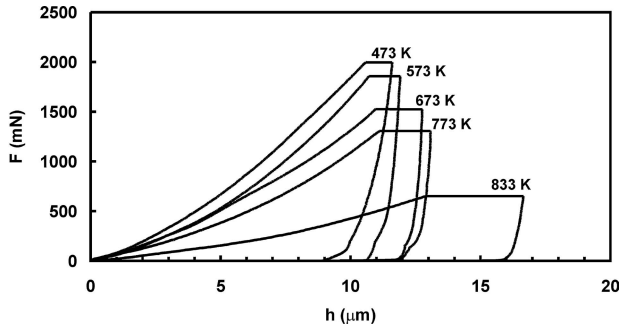

Figure 3 Indentation force F versus indentation depth h for one indentation made at each test temperature on the SiO_2 reinforced P/M 2024 aluminum alloy. The plot shows the decreasing material hardness with increasing test temperature. The length of the horizontal region of each curve indicates the change in indentation depth over 100 seconds at constant indentation load. The trends shown in this figure are typical of the data from all the tests in this study.

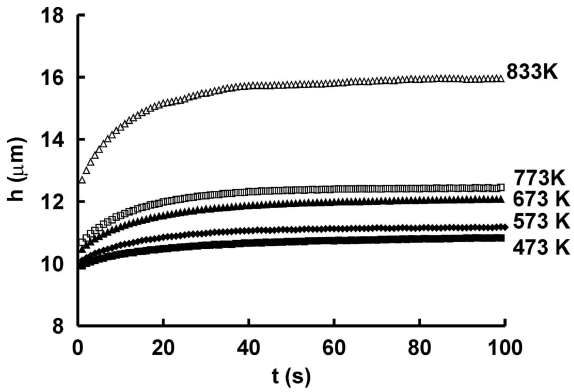

Figure 4 Indentation depth h versus time t during the 100 s constant force segment of the indentation tests shown in Fig. 3. The indentation creep deformation clearly increases with increasing temperature.

The stress-dependence of the steady-state creep rate of particulate reinforced metal matrix composites is a function of the "effective" applied stress defined as the difference between the applied stress and σ_{th}. The steady-state creep rate for particulate-reinforced aluminum matrix composites usually displays temperature- and stress-dependences that are different than what would be expected if the operative deformation mechanism is one of climb-limited dislocation glide (i.e. power-law creep). This suggests that the presence of the reinforcing particles causes a complex local stress state to exist within the aluminum matrix and may well preclude the occurrence of steady-state creep deformation.

In this study we investigate the effect of particulate reinforcement on the deformation kinetics of a composite containing a 2024 aluminum alloy matrix fabricated by the Powder Metallurgy (P/M) process. Composites that are reinforced with three types of particles (SiO_2, SiC, and Al_2O_3) are studied over the temperature range from 473 K to 833 K (approximately 0.5 to 0.9 T_{melt}). The constant-load micro-indentation testing technique, described previously [15] and summarized below, is used to perform the high temperature deformation tests. The resulting indentations are observed with Scanning Electron Microscopy (SEM) to evaluate the role of the reinforcing particulates in the deformation process. This paper is the concluding part of a comprehensive study of the use of microindentation to measure the high-temperature deformation kinetics of materials.

1.1. Deformation during high-temperature constant-load indentation

When indentation tests are performed at high temperature with a pyramidal shaped indenter under constant indentation load conditions the indentation depth h

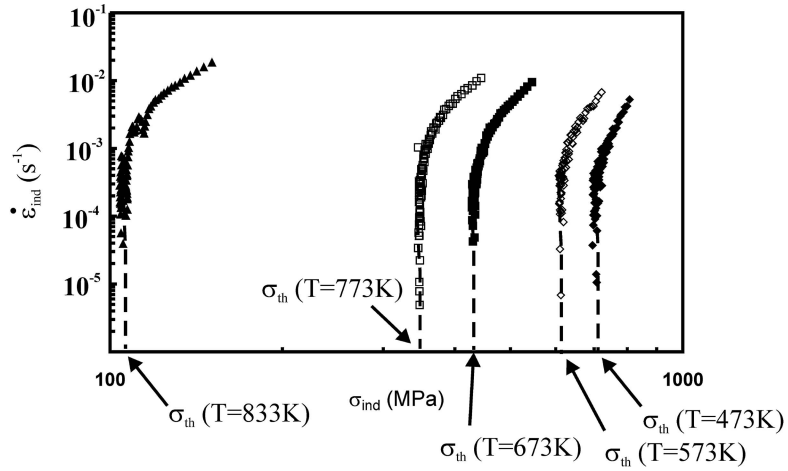

Figure 5 Average indentation strain rate $\dot{\varepsilon}_{ind}$ versus indentation stress σ_{ind} for the indentation tests shown in Figs. 3 and 4. The threshold stress σ_{th} is approximated as the value of σ_{ind} corresponding to $\dot{\varepsilon}_{ind} = 10^{-6}$ sec^{-1}.

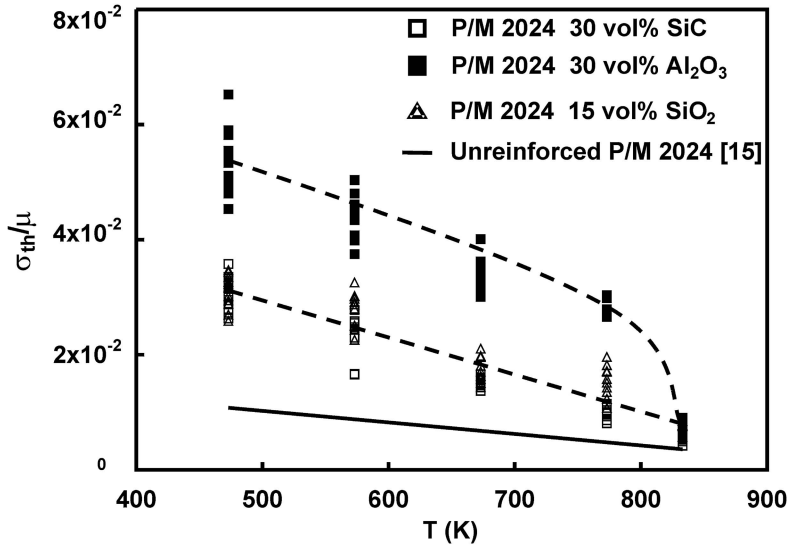

Figure 6 The threshold indentation stress σ_{th}, normalized with respect to the elastic shear modulus μ (Eq. 4), versus temperature T for all the indentation creep tests performed in this study. The three composites studied show essentially the same trend of decreasing σ_{th}/μ with increasing T. At low temperature, σ_{th}/μ is significantly larger for the composite material than for the unreinforced P/M 2024 aluminum alloy (solid line) but at high temperatures the σ_{th}/μ is only slightly larger than that of the unreinforced aluminum alloy.

increases with time as the indenter "creeps" into the tested material. The apparent average indentation strain rate $\dot{\varepsilon}_{ind}$ is expressed in terms of h and the indentation velocity $\dot{h}$ as

$$\dot{\varepsilon}_{ind}(t) = \frac{\dot{h}(t)}{h(t)} \tag{1}$$

Since the tests are performed with a pyramidal shaped indenter, the instantaneous indentation stress σ_{ind}, defined as the indentation load divided by the projected indentation area, decreases with increasing time. Under these conditions $\dot{\varepsilon}_{ind}$ decreases, and approaches zero, with increasing time. The indentation stress that corresponds to the point where $\dot{\varepsilon}_{ind} = 0$ is the indentation threshold stress σ_{th}. The magnitude of σ_{th} depends upon the geometry of the indentation and the microstructure within the indentation plastic zone. When constant-load indentation tests are performed on different materials using indentations of the same depth that are made with the same indenter, differences in the measured σ_{th} indicate differences in the deformed microstructure of the test materials.

Past studies of $\dot{\varepsilon}_{ind}$ performed by using high-temperature constant-load pyramidal indentation, have shown that the dependence of $\dot{\varepsilon}_{ind}$ upon σ_{ind} and temperature T is different than what is observed during steady-state constant-uniaxial stress creep tests. Li *et al.* [16] have shown that $\dot{\varepsilon}_{ind}$ occurs by the mechanism of obstacle-limited dislocation glide over a wide temperature range for most engineering materials including metals and non-metals. This is a reasonable hypothesis since complex, and variable, local stress states exists during the indentation test and these tests are of short time duration compared

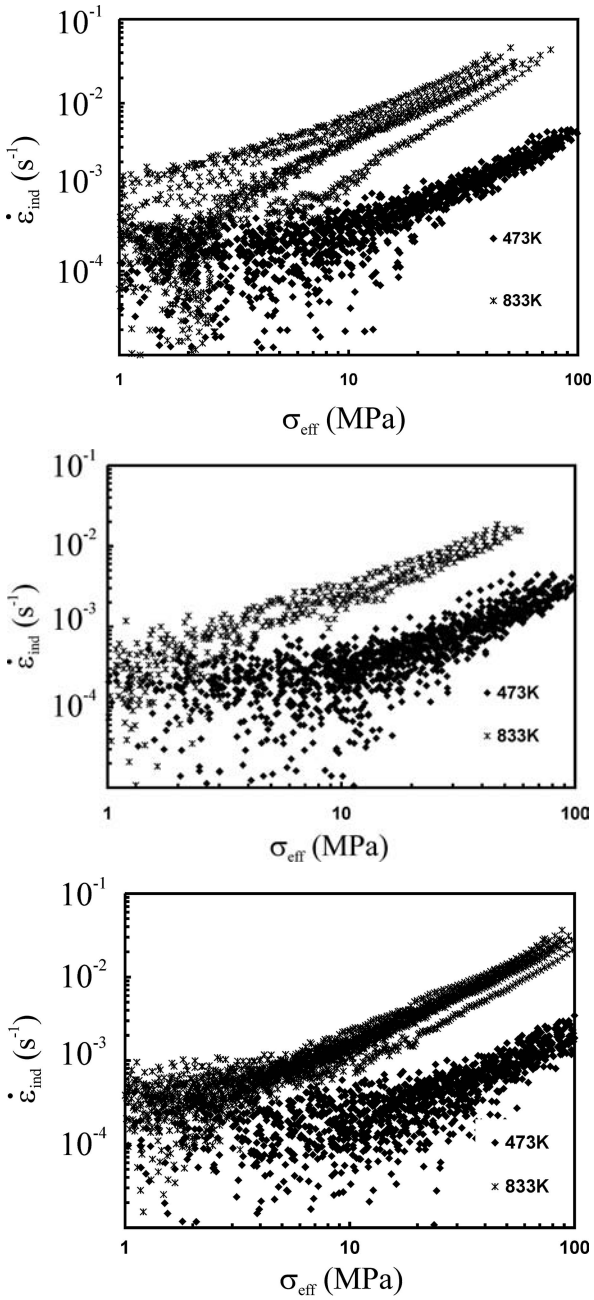

Figure 7 Logarithmic plots of average indentation strain rate $\dot{\varepsilon}_{ind}$ versus effective hardness $\sigma_{eff} = \sigma_{ind} - \sigma_{th}$ for all the indentation creep tests performed on (a) the SiC reinforced composite, (b) the SiO_2 reinforced composite, and (c) the Al_2O_3 reinforced composite. A nonlinear trend exists between log $\dot{\varepsilon}_{ind}$ and log σ_{eff} with the degree of nonlinearity, and the scatter in the data, increasing as the temperature and the effective indentation stress decrease.

to conventional constant-stress creep tests. This approach of expressing $\dot{\varepsilon}_{ind}$ in terms of the mechanism of obstacle-limited dislocation glide has also been taken by other researches to describe the indentation strain-rate sensitivity of ductile metals at room-temperature [17–20].

The shear strain rate $\dot{\gamma}$ resulting from the mechanism of obstacle-limited dislocation glide can be expressed as

$$\dot{\gamma} = \dot{\gamma}_0 e^{\frac{-\Delta G(\tau)}{kT}} \tag{1}$$

TABLE I The chemical composition, in weight percentage, and the average powder diameter, bracketed, of the three particulate reinforced composites studied in this investigation.

	Elements (μm)	SiC reinforced composite	SiO_2 reinforced composite	Al_2O_3 reinforced composite
Matrix	Cu (8–11)	4	4	4
	Mg (7–15)	1.4	1.4	1.4
	Mn (7–15)	0.4	0.4	0.4
	Al (7–15)	Bal.	Bal.	Bal.
Reinforcements	SiO_2 (1–5)	–	16.9	–
	SiC (5)	17.2	–	–
	Al_2O_3 (9.5)	–	–	43.0
Average grain diameter, μm ($\pm$ 1 stand. dev.)		9.6 ($\pm$0.9)	11.9 ($\pm$1.3)	10.8 ($\pm$0.9)

where $\dot{\gamma}_0$ is a material constant, usually taken as 10^6 sec^{-1}[21], k is Boltzmann's constant, T is the absolute temperature and $\Delta G(\tau)$ is the stress-dependent thermal energy required for a dislocation to overcome an obstacle. The average equivalent indentation shear stress can be related to the average indentation stress as [16]

$$\tau_{ind} = \frac{\sigma_{ind}}{3\sqrt{3}} \tag{2}$$

and the average equivalent indentation shear strain rate can be expressed in terms of the indentation depth and velocity $\dot{h}$ as

$$\dot{\gamma}_{ind} = \sqrt{3}\dot{\varepsilon}_{ind} \tag{3}$$

Pyramidal indentation tests performed under constant indentation load will produce trends of decreasing $\dot{\varepsilon}_{ind}$ and σ_{ind} with increasing time. Eqs. 1 to 3 can then be applied to determine $\Delta G(\tau)$ as a function of σ_{ind} and the resulting $\Delta G(\tau)$ versus τ_{ind} trend characterizes the average dislocation/obstacle interactions that control the indentation strain rate. Extrapolation of this trend to $\tau_{ind} = 0$ gives an estimation of the activation energy ΔG_0 of the obstacles that limit the deformation process.

2. Procedure

Three aluminum-based particulate reinforced composite material (Table I) were fabricated for this study by the Powder Metallurgy (P/M) technique [22, 23]. The matrix of all the composites was of a 2024 aluminum alloy composition and was prepared by mixing powders of pure aluminum, copper, magnesium, and manganese in the proportions given in Table I. The metal powders were from 7 to 15 μm in diameter (as stated by the manufacturers). The mixed powders were then divided into three groups and to each group was added one of the three particle types (SiO_2, SiC, or Al_2O_3) in amounts that resulted in 16.9, 17.2, and 43.8 weight percent respectively. The average

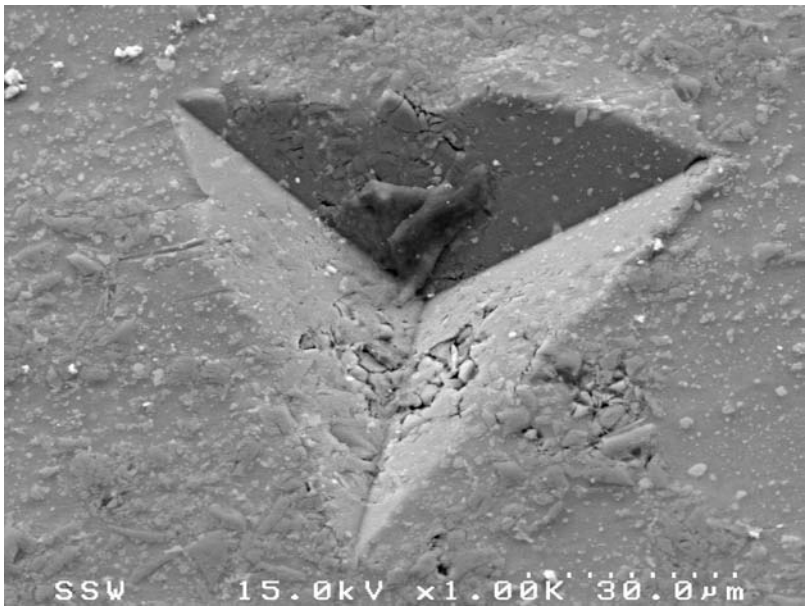

Figure 8 Scanning electron micrograph of an indentation made in SiC reinforced 2024 P/M aluminum alloy composite indented at 673 K. Cracking of the reinforcing particles and interfacial debonding occurs within, and in the region immediately surrounding, the indentation but does not occur in the regions away from the indentation. This indicates that the cracking and interfacial debonding is a result of the indentation deformation.

diameter of the reinforcing particles was between 1 and 10 μm (as stated by the manufacturers). Cylindrical samples were made from each powder mixture by cold-pressing followed by sintering in vacuum at 873 K for several hours. After sintering, the samples were hot-pressed in air at 823 K.

The as-fabricated composites were prepared for metallographic examination by mechanical grinding followed by successively finer polishing steps culminating in a 0.25 μm finish. The average grain diameter of each of the composites was measured from optical micrographs (Fig. 1) taken from regions of the samples where subsequent indentation tests were performed. The measured average grain diameter is given in Table I.

The reinforcing particles are located around the periphery of the original aluminum powders. This is shown clearly by the higher magnification SEM image of the SiC reinforced composite (Fig. 2). The local areal fraction of the reinforcing particulates in the region where the indentation tests were performed was measured from optical micrographs and was found to be 30, 15, and 30% for the SiC, SiO_2 and Al_2O_3 reinforced composites respectively.

Microindentation tests were performed on polished surfaces of the composite samples at 473, 573, 673, 773, and 833 K using a high-temperature Microtest II indentation hardness tester (Micro Materials Ltd, Wrexham U.K.) [24–26]. The instrument is contained in a cabinet located on an air table. A mildly reducing atmosphere of Ar 2% H_2 gas is maintained in the cabinet to minimize oxidation of the specimen during the indentation tests.

Between 10 and 15 indentation tests were performed on each sample at each temperature. The tests were performed in order of ascending temperature and the samples were not cooled between testing at each temperature. The samples were held at each temperature for approximately five hours to ensure that both the sample and the indenter, located several micrometers away from the sample, were at the same temperature before indentation tests commenced. Each test began by applying an indentation load at a rate of 50 mN/s until an indentation depth of between 10 and 13 μm was reached. The indentation load was then held constant for 100 seconds during which time the indentation depth was recorded at half-second intervals. The indentation depth data were corrected for the effects of thermal drift and compliance of the indentation load frame.

3. Results

The indentation force F versus indentation depth h is shown in Fig. 3 for one test performed at each temperature on the SiO_2 reinforced composite. These curves are typical of those obtained for all the indentation tests performed in this study. Fig. 4 shows the increasing h as a function of time during the 100-second hold period of the tests shown in Fig. 3. The indentation velocity $\dot{h}$ is large at the start of each test and decreases with increasing time. This is due to the decrease in σ_{ind} that results as h increases under constant indentation load.

The average indentation strain rate $\dot{\varepsilon}_{\text{ind}}$ (Eq. 1) is plotted versus the instantaneous indentation stress $\sigma_{\text{ind}} = F / 24.5\ h^2$ in Fig. 5 for the tests shown in Fig. 4. The data trends are extrapolated to $\dot{\varepsilon}^{\text{ind}} = 10^{-6}\ s^{-1}$ to approximate the threshold hardness, σ_{th}, below which no measurable $\dot{\varepsilon}_{\text{ind}}$ occurs.

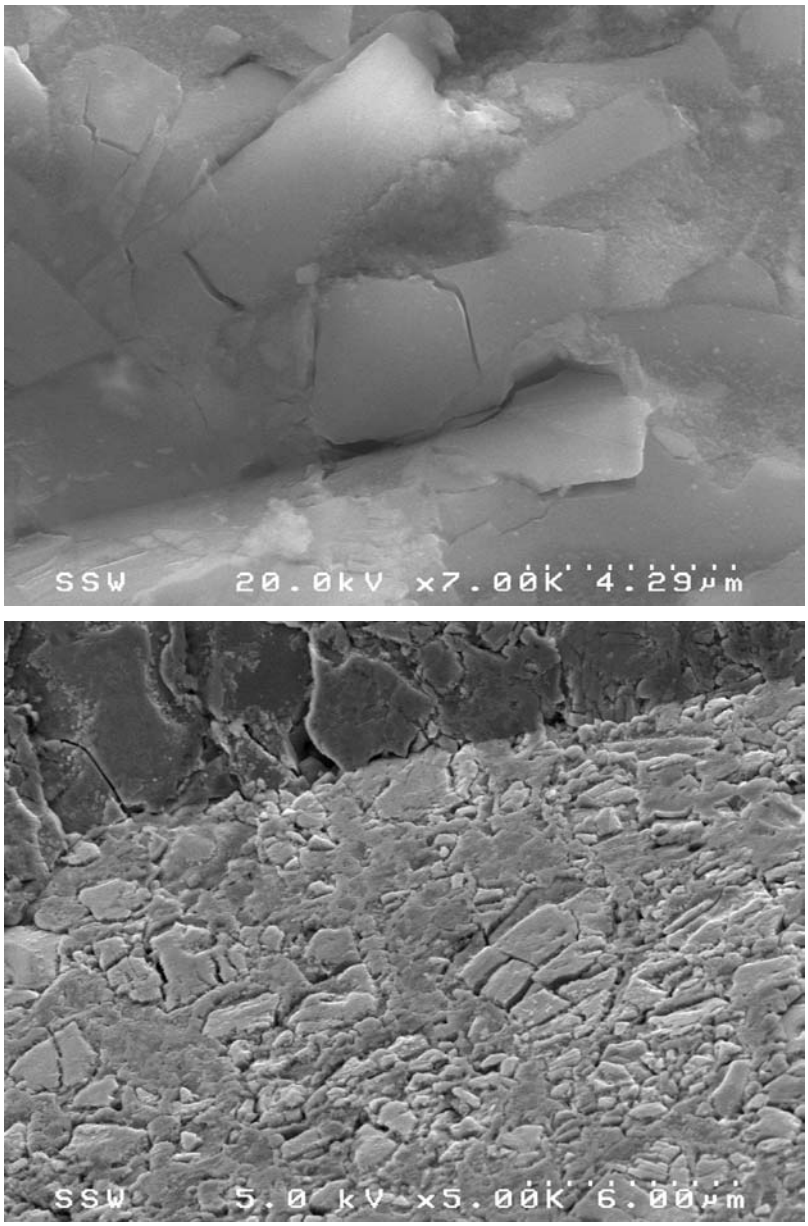

Figure 9 Scanning electron micrographs of the indented region of the SiC reinforced 2024 P/M aluminum alloy composite indented at (a) 573 K and (b) 833 K. Cracking of the particles and interfacial debonding occurs at both temperatures but the amount of particle cracking and interfacial debonding increases with increasing indentation temperature.

A plot of σ_{th}, normalized with respect to the elastic shear modulus μ of pure aluminum, versus the temperature is shown in Fig. 6 for the three composites studied. A line representing the σ_{th}/μ versus T for unreinforced P/M fabricated 2024 aluminum alloy [15] is also shown for comparison. The term μ is expressed, in units of MPa, as [21]

$$\mu(T) = 25400\left[1 - 0.5\frac{T-300}{933}\right] \tag{4}$$

The three composites have significantly higher σ_{th} at all temperatures than the unreinforced aluminum alloy however the difference in σ_{th} decreases with increasing temperature. The Al_2O_3 reinforced composite has the highest σ_{th} of the three composites.

Fig. 7 shows $\dot{\varepsilon}_{ind}$ versus the effective indentation stress; $\sigma_{eff} = \sigma_{ind} - \sigma_{th}$ for the three composites tested at 473 K and 833 K. These temperatures are the upper- and lower-bounds of the test temperatures of this study. The composites all show a non-linear dependence of $\dot{\varepsilon}_{ind}$ upon σ_{eff}, and the degree of non-linearity increases with decreasing temperature.

Fig. 8 shows a scanning electron micrograph of an indentation made in the SiC reinforced composite at 673 K. The micrograph shows clearly that interfacial debonding occurs in the interior, and around the periphery, of the indentation. This indicates that indentation deformation is accompanied by considerable

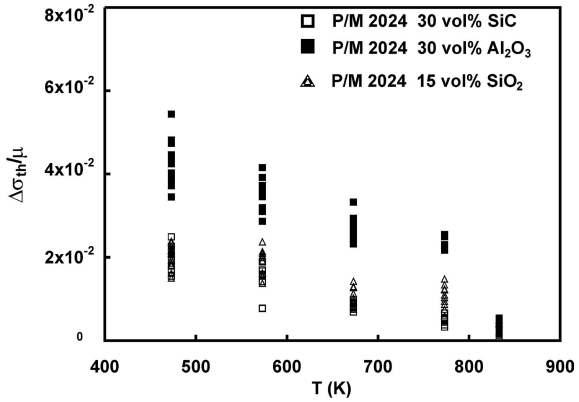

Figure 10 The difference in threshold indentation stress $\Delta\sigma_{th}/$, between the particulate reinforced P/M 2024 materials of this study and the previously reported unreinforced P/M 2024 alloy [12], versus temperature T. The magnitude of $\Delta\sigma_{th}/\mu$ indicates the effect of the particulate reinforcement on the observed threshold indentation stress. The particulate reinforcements have a greater affect on σ_{th} at the low temperatures and the Al_2O_3 particulates are the most effective at increasing $\Delta\sigma_{th}$.

debonding and cracking of the reinforcing particles. While extensive cracking and interfacial debonding of the reinforcing particles occurs at all the test temperatures, the amount of debonding and particle cracking increases with increasing temperature. This is shown by the SEM images in Fig. 9 where the surfaces of indentations made on the SiC reinforced composite at 573 and 833 K are depicted.

4. Discussion

We now analyse in more detail the temperature dependence of σ_{th} and discuss the mechanism responsible for σ_{th} in the composite materials. We then analyse the dependence of $\dot{\varepsilon}_{ind}$ upon σ_{eff} and T to determine the apparent activation energy ΔG_0 of the obstacles that control $\dot{\varepsilon}_{ind}$. We compared the temperature dependence of σ_{th} and ΔG_0 with that which was previously reported for the unreinforced P/M 2024 aluminum alloy and discuss the possible dislocation/obstacle interactions that control these parameters.

4.1. The dependence of σ_{th} upon temperature

The σ_{th}/μ of the composites is larger in magnitude than that of the unreinforced P/M 2024 aluminum alloy and the difference in magnitude is largest at the low temperatures (Fig. 6). Both materials have the same P/M 2024 aluminum alloy matrix which contains, in addition to oxide particles inherent with the P/M fabrication process, $CuAl_2$ precipitates whose quantity decreases with increasing temperature up to about 773 K. We can therefore assume that the effect of the $CuAl_2$ precipitates on σ_{th}/μ is the same for the composite material as it is for the unreinforced P/M 2024 alloy. Fig. 10 shows $\Delta\sigma_{th}/\mu$ versus temperature where $\Delta\sigma_{th}/\mu$ is the difference in σ_{th}/μ between the composites and the unreinforced alloy.

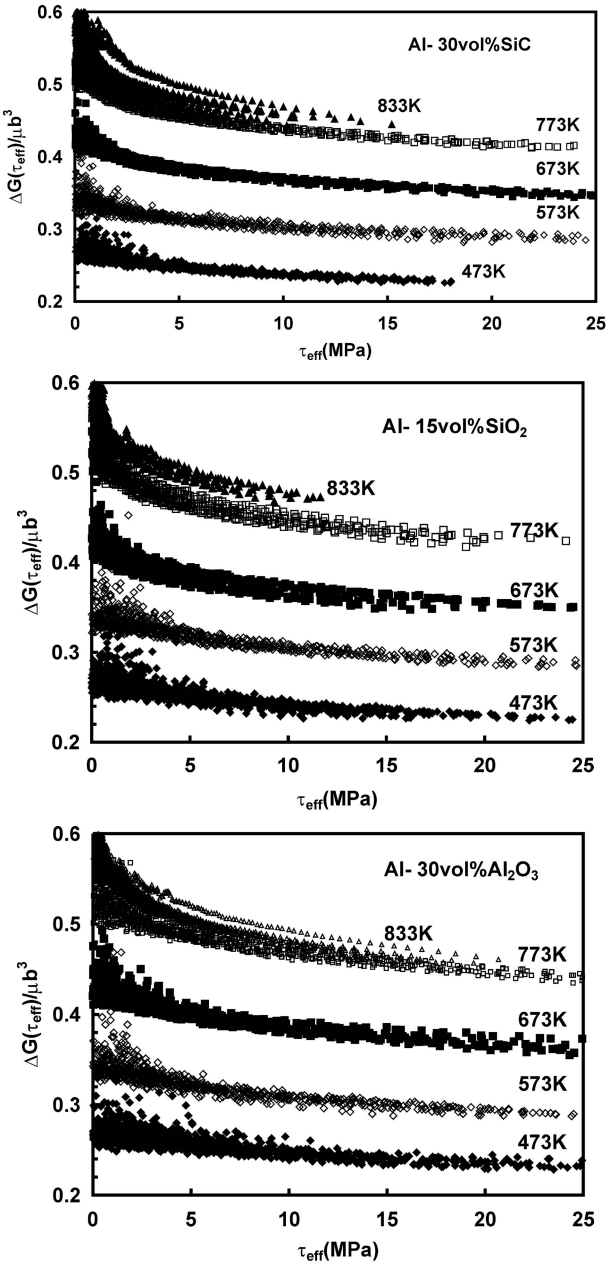

Figure 11 Apparent thermal energy $\Delta G(\tau_{eff}$ (Eq. 1)) of $\dot{\varepsilon}_{ind}$, normalized with respect to strain energy of a dislocation μb^3, versus the effective indentation shear stress τ_{eff} (Eq. 2) for the indentation tests performed at each test temperature on (a) the SiC reinforced composite, (b) the SiO_2 reinforced composite, and (c) the Al_2O_3 reinforced composite.

Fig. 10 indicates the contribution of the particulate reinforcements to σ_{th}/μ.

During the indentation of the composite material, the indenter contacts many particles (Figs. 8 and 9). This has the effect of distributing the indentation load over a larger surface area and reducing the effective stress felt by the aluminum alloy matrix. While particle cracking and interfacial debonding occur at all the test temperatures, the extent of cracking and debonding increases with temperature and is different for one type of reinforcement than another. The Al_2O_3 particulate reinforced composite has the largest magnitude of $\Delta\sigma_{th}/\mu$ and displays the least

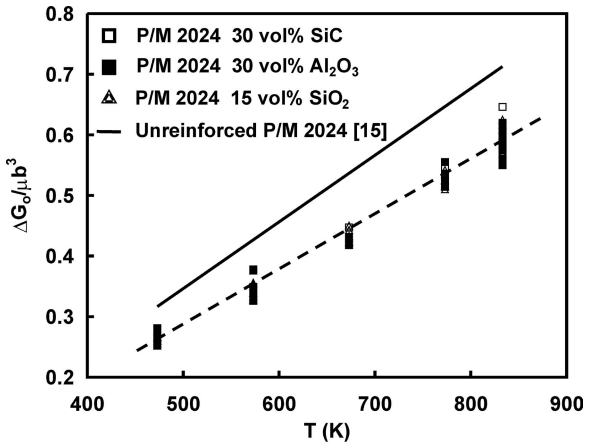

Figure 12 The apparent normalized activation energy $\Delta G_0/\mu b^3$ of the indentation rate controlling obstacle, versus temperature T for the three composites tested. The three composites tested all followed the same $\Delta G_0/\mu b^3$ versus T trend with the value of $\Delta G_0/\mu b^3$ being lower than the previously reported value for the unreinforced P/M 2024 alloy.

amount of debonding at matrix/particle interfaces. We therefore conclude that variations in the trend of $\Delta\sigma_{th}/\mu$ versus temperature shown in Fig. 10 are due to the tendencies for the different particles to crack and debond during indentation.

The magnitude of our measured ε_{ind} and our observation that σ_{th}/μ decreases with increasing temperature is consistent with what is observed during the uniaxial stress deformation of similar composites [7–9]. The magnitude of σ_{th} that we report is, however, considerably larger than that reported from uniaxial stress tests. We attribute this to the difference in the local stress state during pyramidal indentation compared to that during uniaxial stress testing and to the fact that the indentation tests are of much shorter duration and therefore involve a non-steady state obstacle-limited dislocation glide deformation mechanism (Section 1). This is discussed further in the following section.

4.2. The dependence of ΔG_0 upon temperature

Fig. 11 shows, $\Delta G(\tau_{ind})$ calculated from Eq. 1, versus τ_{ind} for the three composites at each temperature tested. Extrapolation of the data trends to $\tau_{ind} = 0$ gives the apparent activation energy, ΔG_0, of the obstacles that control $\dot{\varepsilon}_{ind}$. The $\Delta G_0/\mu b^3$ values, estimated in this manner, are plotted versus temperature in Fig. 12. Included in the plot is a line indicating the trend for the unreinforced P/M 2024 aluminum alloy [12]. ΔG_o increases from approximately $0.25\mu b^3$ at 473 K to $0.60\mu b_3$ at 833 K. This falls within the expected range for the activation energy of medium strength obstacles, such as dislocation/dislocation interactions or dislocation/weak particle interactions [19]. While the three composites show essentially the same trend of $\Delta G_o/\mu b^3$ versus temperature, and the temperature dependence of this parameter is the same as that of the unreinforced P/M 2024 alloy, the magnitude of $\Delta G_o/\mu b^3$ is consistently lower than that of the unreinforced alloy. This suggests that, while the reinforcing particles result in a higher threshold stress (as discussed in Section 4.1) when the indentation stress exceeds σ_{th}, the obstacles that control $\dot{\varepsilon}_{ind}$ are weaker in the composites than in the unreinforced alloy. We have observed that considerable cracking occurs in the reinforcing particles and at the particle/matrix interfaces especially at high temperature. This means that the composite samples may have more porosity and free surfaces in the indented regions than the unreinforced alloy. This is especially probable at the boundaries of the prior aluminum powders where the reinforcing particles are clustered.

5. Conclusion

Constant-load pyramidal indentation tests were performed, at temperatures from 473 K to 833 K, on P/M fabricated 2024 aluminum alloy reinforced with particles of SiO_2, SiC, and Al_2O_3 to investigate the kinetics of the deformation process.

The composites all displayed apparent threshold stress σ_{th} below which the indentation rate was essentially zero. The σ_{th}/μ, decreased with the increasing temperature but was larger than that of an unreinforced P/M 2024 aluminum alloy particularly at the lower temperatures. We attribute this to load-transfer that occurs when the indenter contacts the reinforcing particles. This load-transfer reduces the effective stress felt by the aluminum alloy matrix. While particle cracking and interfacial debonding was observed in the indented microstructure of all the samples at all temperatures tested, the amount of cracking and debonding increased with increasing temperature. This, along with the decreasing amount of $CuAl_2$ precipitates present in the matrix with increasing temperature, is the cause of the observed decrease in σ_{th}/μ with increasing temperature.

The apparent activation energy ΔG_0 of the average indentation strain rate ε_{ind} increased from 0.25 μb^3 at 473 K to $0.60\mu b^3$ at 833 K. These values are within the range of medium strength obstacles to dislocation glide such as weak particle or dislocation/dislocation interactions but are lower in magnitude than the value measured on unreinforced P/M 2024 alloy using the same test techniques [12]. We therefore conclude that, while particulate reinforcement raises the σ_{th}, when the indentation stress exceeds σ_{th}, $\dot{\varepsilon}_{ind}$ is limited by the obstacle-dislocation interactions that are slightly weaker than those in the unreinforced alloy. This is probably related to the fact that extensive cracking and interfacial debonding occurs in the composite material at high temperature resulting in internal porosity which facilitates $\dot{\varepsilon}_{ind}$.

The results of this investigation have demonstrated the usefulness of high-temperature microindentation to study the details of the high-temperature deformation of complex multiphase materials.

Acknowledgments

The authors wish to thank Mr. R.N. Saraf and F. Azarmi for fabricating the composite specimens used in this study. We also wish to acknowledge the Natural Science and Engineering Research Council of Canada who provided financial support for this research.

References

1. M. FINOT, Y-L. SHEN, A. NEEDLEMAN and S. SURESH, *Metall. Trans.* **A41** (1994) 885.
2. S. F. CORBIN and D. S. WILKINSON, *Acta Metall. Mater.* **42** (1994) 1311.
3. T. CHRISTMAN, A. NEEDLEMAN and S. SURESH S, *Acta Metall. Mater.* **37** (1989) 3029.
4. G. BAO, *Acta Metall. Mater.* **40** (1992) 2547.
5. R. J. ARSENAULT, L. WANG and C. R. FENG, *Acta Metall Mater.* **39** (1991) 47.
6. P. M. SINGH and J. J. LEWANDOWSKI, *Trans.* **24A** (1993) 2531.
7. W.-J. KIM and O. D. SHERBY, *Acta Mater.* **48** (2000) 1763.
8. W. J. KIM, J. H. YEON, D. H. SHIN and S. H. HONG, *Mat. Sci. Eng.* **A269** (1999) 142.
9. W.-J. KIM, D.-W. KUM and H.-G. JEONG, *J. Mater. Res.* **16** (2001) 2429.
10. D. S. WILKINSON and E. ARTZ, *Acta metall* **34** (1986) 1893.
11. R. S. W. SHEWFELT and L. M. BROWN, *Phil. Mag.* **35** (1977) 945.
12. E. ARTZ, G. DEHM, P. GUMBSCH, O. KRAFT and D. WEISS, *Prog. Mater. Sci.* **46** (2001) 283.
13. K. T. CONLON and D. S. WILKINSON, *Mat. Sci. Eng.* **A317** (2001) 108.
14. D. S. WILKINSON, W. POMPE and M. OESCHNER, *Prog. Mater. Sci.* **46** (2001) 379.
15. V. BHAKHRI and R. J. KLASSEN, submitted to *J. Mat. Sci.* (April 2005).
16. W. B. LI, J. L. HENSHALL, R. M. HOOPER and K. E. EASTERLING, *Acta Metall. Mater.* **39** (1991) 3099.
17. S. SAIMOTO, B. J. DIAK and K. R. UPADHYAYA, *Mater. Sci. Engng.* **A234 – A236** (1997) 1015.
18. B. J. DIAK and S. SAIMOTO *Mater. Sci. Engng.* **A319 – A321** (2001) 909.
19. A. ELMUSTAFA and D. S. STONE, *J. Mech. Phys. Solids* **51** (2003) 357.
20. R. J. KLASSEN, B. J. DIAK and S. SAIMOTO, *Mater. Sci. Engng.* **A387 – 389** (2004) 297.
21. H. J FROST and M. F. ASHBY, "Deformation-Mechanism Maps" (Pergamon Press, Oxford, 1982) p. 21.
22. R. N. SARAF, M.E.Sc "Creep Properties of SiO_2 and NiAl Reinforced Composites" (Thesis University of Western Ontario, London Canada, 2003).
23. F. AZARMI, M.E.Sc "Creep Behaviour of Al-Based Composites Made By The P/M Technique" (Thesis University of Western Ontario, London Canada, 2002).
24. J. F. SMITH and S. ZHANG, *Surf. Engng.* **16** (2000) 143.
25. B. D. BEAKE and J. F. SMITH, *Philos. Mag.* **A8** (2002) 2179.
26. B. D. BEAKE, S. R. GOODES and J. F. SMITH, Z. Metallkd. **7** (2003) 798.

Received 24 September 2004
and accepted 14 March 2005